Noninvasive mapping of pancreatic inflammation in recent-onset type-1 diabetes patients

Jason L. Gaglia[a,1], Mukesh Harisinghani[b,c,1], Iman Aganj[c], Gregory R. Wojtkiewicz[b,c], Sandeep Hedgire[b,c], Christophe Benoist[d,e], Diane Mathis[d,e,2,3], and Ralph Weissleder[b,c,2,3]

[a]Joslin Diabetes Center, Boston, MA 02215; [b]Center for Systems Biology and [c]Department of Radiology, Massachusetts General Hospital, Boston, MA 02114; [d]Division of Immunology, Department of Microbiology and Immunobiology, Harvard Medical School, Boston, MA 02115; and [e]Evergrande Center for Immunologic Diseases, Harvard Medical School and Brigham and Women's Hospital, Boston MA, 02115

Contributed by Diane Mathis, January 5, 2015 (sent for review December 22, 2014)

The inability to visualize the initiation and progression of type-1 diabetes (T1D) noninvasively in humans is a major research and clinical stumbling block. We describe an advanced, exportable method for imaging the pancreatic inflammation underlying T1D, based on MRI of the clinically approved magnetic nanoparticle (MNP) ferumoxytol. The MNP-MRI approach, which reflects nanoparticle uptake by macrophages in the inflamed pancreatic lesion, has been validated extensively in mouse models of T1D and in a pilot human study. The methodological advances reported here were enabled by extensive optimization of image acquisition at 3T, as well as by the development of improved MRI registration and visualization technologies. A proof-of-principle study on patients recently diagnosed with T1D versus healthy controls yielded two major findings: First, there was a clear difference in whole-pancreas nanoparticle accumulation in patients and controls; second, the patients with T1D exhibited pronounced inter- and intrapancreatic heterogeneity in signal intensity. The ability to generate noninvasive, 3D, high-resolution maps of pancreatic inflammation in autoimmune diabetes should prove invaluable in assessing disease initiation and progression and as an indicator of response to emerging therapies.

autoimmune diabetes | magnetic resonance imaging | nanoparticle | insulitis | pancreas

Type 1A diabetes (T1D) is a chronic autoimmune disease characterized by destruction of the insulin-producing beta cells of the pancreatic islets of Langerhans. During an initial occult phase, immunological tolerance breaks down and autoimmunity sets in, leading to leukocyte infiltration of the islets, which reduces the number and function of insulin-producing beta cells. The overt phase of clinical diabetes starts once sufficient damage has been done that insulin production is insufficient for proper glucose homeostasis. Despite advances in the identification of disease-relevant autoantigens and susceptibility genes, most clinical trials performed so far have reported no or only a modest impact on disease course (1). This lack of successful outcomes may reflect our relative ignorance of T1D pathogenesis in humans, much of our understanding of the disease having come from animal models. This situation is, to a large extent, a consequence of the difficult-to-impossible access to pancreatic tissue during and after the development of diabetes in patients.

As a consequence, much effort has been devoted to identifying readily measurable biomarkers of the autoimmune state and of the progression of islet destruction. The most widely adopted indicator is autoantibodies (autoAbs) targeting islet proteins such as insulin, GAD2 (also known as "glutamic acid decarboxylase 65," GAD65), PTPRN ("islet cell antigen 512," IA2), and SLC30A8 ("zinc transporter-8," ZNT8). The presence and titer of autoAbs identifies individuals at elevated risk for developing clinical disease, those with autoAbs against multiple targets being at particularly high risk (2–5). However, autoAbs are persistent, and their presence informs on an aggregate risk of progression rather than on the status of autoimmunity or islet destruction at a given time.

An indicator of leukocyte infiltration of the pancreatic islets would be a more direct disease biomarker. Inflammation of human islets has been difficult to evaluate histologically, because access to material is invasive and therefore difficult. As recently reviewed (6, 7), very limited numbers of individuals have been analyzed (e.g., ref. 8), many in conditions of questionable relevance to typical pathogenesis, e.g., patients with very long-lasting T1D in whom the autoimmune attack may have waned, or individuals who died of acute ketoacidosis. In addition, the histological evaluation can be complicated by variations in sample procurement and processing. In general, insulitis seems to be more frequent in high-risk individuals or in patients presenting with T1D at a young age, but may be less extensive than in the nonobese diabetic (NOD) mouse model (likely reflecting the much faster progression of diabetes in the latter).

In rodent models of T1D, insulitis is accompanied by changes in the pancreatic microvasculature (9–11). Similarly, there is evidence of increased vascular permeability as a consequence of the inflammatory process involving the islets of patients with T1D (12). The activation of mononuclear phagocytes is an early and integral part of the local inflammatory process in both cases (13, 14). We previously showed that i.v. injection of dextran-coated

Significance

We describe a readily exportable method for noninvasive imaging of the pancreatic inflammation underlying type-1 diabetes (T1D), based on MRI of the clinically approved magnetic nanoparticle ferumoxytol. This approach, which reflects nanoparticle uptake by macrophages in the inflamed pancreatic lesion, has been validated rigorously in mouse T1D models. Methodological advances reported here include extensive optimization of image acquisition and improved MRI registration and visualization technologies. A proof-of-principle study revealed a clear difference in whole-pancreas nanoparticle accumulation in patients with recent-onset T1D versus healthy controls and pronounced intra- and interpancreatic signal heterogeneity in patients. Noninvasive generation of 3D, high-resolution maps of pancreatic inflammation should prove invaluable in assessing T1D progression and as an indicator of response to therapy.

Author contributions: J.L.G., M.H., C.B., D.M., and R.W. designed research; J.L.G., M.H., I.A., G.R.W., and S.H. performed research; J.L.G., M.H., I.A., G.R.W., and S.H. analyzed data; and J.L.G., M.H., I.A., C.B., D.M., and R.W. wrote the paper.

The authors declare no conflict of interest.

[1]J.L.G. and M.H. contributed equally to this work.

[2]D.M. and R.W. contributed equally to this work.

[3]To whom correspondence may be addressed. Email: dm@hms.harvard.edu or rweissleder@mgh.harvard.edu.

This article contains supporting information online at www.pnas.org/lookup/suppl/doi:10.1073/pnas.1424993112/-/DCSupplemental.

magnetic nanoparticles (MNPs) phagocytosed by macrophages followed by MRI could be used to visualize the pancreatic inflammatory process in the NOD mouse model and transgenic derivatives thereof (11, 15, 16). Based on these observations, we performed a small human feasibility study with a now-discontinued nanoparticle, ferumoxtran-10 (Combidex). Results from this study suggested that pancreas uptake of these nanoparticles might be a useful, noninvasive indicator of islet inflammation in human patients with T1D (17).

Here, we report crucial technological advances in our approach to quantitative, noninvasive imaging of pancreatic inflammation by nanoparticle-based visualization of local macrophage accumulation. These novelties include a newer, clinically approved nanoparticle, imaging at a higher field strength, optimized pulse sequences, and improved registration and visualization tools, analogous to those used in brain mapping. These advances combine to yield a method that has considerably better resolution and discrimination and is readily exportable. We document measurably increased levels of pancreatic inflammation, as well as pronounced regional heterogeneity, in patients with recent-onset T1D.

Results

Discontinuation of ferumoxtran-10 as a human imaging agent prompted us to explore the suitability of ferumoxytol (Feraheme), a nanoparticle with a shorter intravascular half-life of ~14.5 h that is approved by the Food and Drug Administration (FDA) for iron-replacement therapy (www.accessdata.fda.gov/drugsatfda_docs/label/2009/022180lbl.pdf) (18). Advancing beyond our previous study on patients with recent-onset T1D (17), the goal here was to develop analytical MRI tools that would be robust, clinically approved, and, perhaps most important, deployable across different sites for longitudinal analysis of patients.

Image Acquisition, Analysis, and Mapping. The desired advances proved nontrivial, because moving to a higher field strength (3T) to yield a stronger signal resulted in increased susceptibility from adjacent bowel structures as well as an accentuation of motion artifacts. In addition, we found that ferumoxytol, although still superparamagnetic, had effects on MR images considerably different from those of ferumoxtran-10, presumably because of different relaxivities resulting from different coatings. Therefore we carefully optimized the type of pulse sequences acquired, timing parameters of these pulse sequences, spatial resolutions, motion-compensation techniques, imaging time to minimize artifacts, and optimum dose of ferumoxytol. These iterative enhancements greatly improved the pancreatic signal and spatial resolution.

Fig. 1 summarizes the image acquisition and analysis sequence. Differently weighted MRI pulse sequences were acquired as 3D datasets and then were used as single slices or 3D volumes to display pancreatic anatomy (T1-weighted sequence) or uptake of nanoparticles (related to differences in T2*-weighted sequences). Because 1/T2* (R2*) has a linear relationship with tissue iron concentration (19), the change in R2* (ΔR2*) directly reflects changes in ferumoxytol accumulation in macrophages. For easier visualization, we color-coded the ΔR2* changes. All pancreata in our study could be segmented easily based on margin delineation of pancreatic parenchyma against surrounding fat.

One major application of this analytical technique in the context of T1D is likely to be mapping inflammatory changes over time and/or in response to drug treatments. Because pancreatic volumes in patients with T1D may change over time (17, 20–22), and patients are positioned differently over multiple imaging sessions, it became necessary to develop a fusion algorithm that merges volumes onto each other. We were inspired by algorithms first developed for brain mapping (23) and thus adapted them to pancreatic fusions (Movie S1). We also developed visualization methods to interrogate easily nanoparticle uptake throughout the entire pancreas.

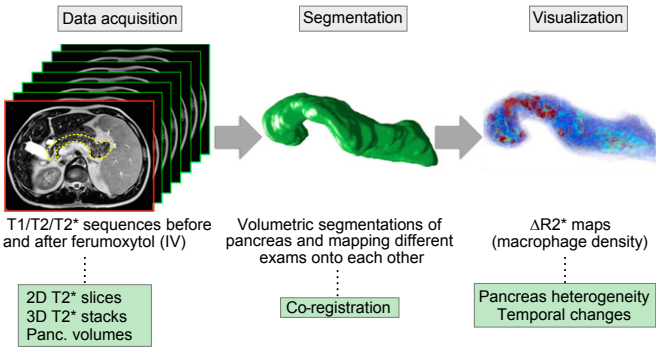

Fig. 1. Scheme of image analysis and visualization. Abdominal MR images were acquired as T1-, T2-, and T2*-weighted image stacks (*Left*). The pancreas is segmented manually on T1-weighted images (yellow dotted line) and propagated through the entire T1 and T2 stack, between stacks, and after i.v administration of ferumoxytol. Segmented images are volumized and registered to each other, first rigidly and then deformably (*Center*). Finally, ΔR2* maps reflecting areas of nanoparticle uptake by macrophages are computed by displaying the difference of pixel R2* values in the "before" and "after" images (*Right*). A pseudocolor scale then is used to represent the ΔR2* values.

Intrapancreatic Heterogeneity. This approach allowed far better evaluation of the heterogeneity of probe accumulation and thus of the distribution of inflammation across the pancreas. Fig. 2 provides illustrative examples of datasets collected from a patient with recent-onset T1D and a control individual (see also Fig. S1 and Movies S2*A* and S2*B* for individual sections covering the entire pancreas). There was markedly higher pancreatic nanoparticle accumulation in the T1D subject, on single sections as well as throughout the entire pancreatic volume. Probe concentration in the diabetic patient was very heterogeneous, with some pancreas regions appearing entirely devoid of signal, consistent with the heterogeneity of the distribution of insulitis in the NOD model and in patients with T1D (24, 25). These findings were seen in other T1D study subjects as well (Fig. S2).

For better visualization and localization of the inflammatory changes, surface projections were generated computationally by projecting the insulitis (ΔR2*) images to the pancreatic surfaces extracted from the T1 images, thereby showing the near-surface ΔR2* values on the surfaces. The pancreatic surfaces then were "inflated" to allow easier inspection of the regions within the pancreas where the nanoparticles have accumulated (Fig. 3). In the example shown in Fig. 3, probe concentration was highest in the head and body of the pancreas, with much less occurring in the tail (also see Movie S3). Once again, there was little or no nanoparticle accumulation in control individuals, and their pancreata appeared essentially homogenous.

Next, we applied this procedure to assessing the extent and distribution of pancreatic inflammation in 21 subjects, including 11 with autoAb-positive, recent-onset T1D (with imaging performed 50–193 d after diagnosis) and 10 healthy controls (summarized in Table S1). Fig. 4 presents volumetric plots of the ΔR2* values of individual patients, slightly blurred for better visualization and cross-cohort comparison of the spatial distribution of nanoparticle accumulation. There was considerable heterogeneity within the pancreas and also among the individual T1D subjects. One patient (Fig. 4, *Upper Left*) had massive inflammation of the head and body of the pancreas but less inflammation of the tail; the remainder of the patients had more restrained levels of inflammation. The spatial distribution was heterogeneous in 5 (P1, P2, P6, P7, and P8) of the patients and was more homogenous in the remainder. There were no evident correlations between the ΔR2* map features and the acquired clinical characteristics of individual subjects (Table 1).

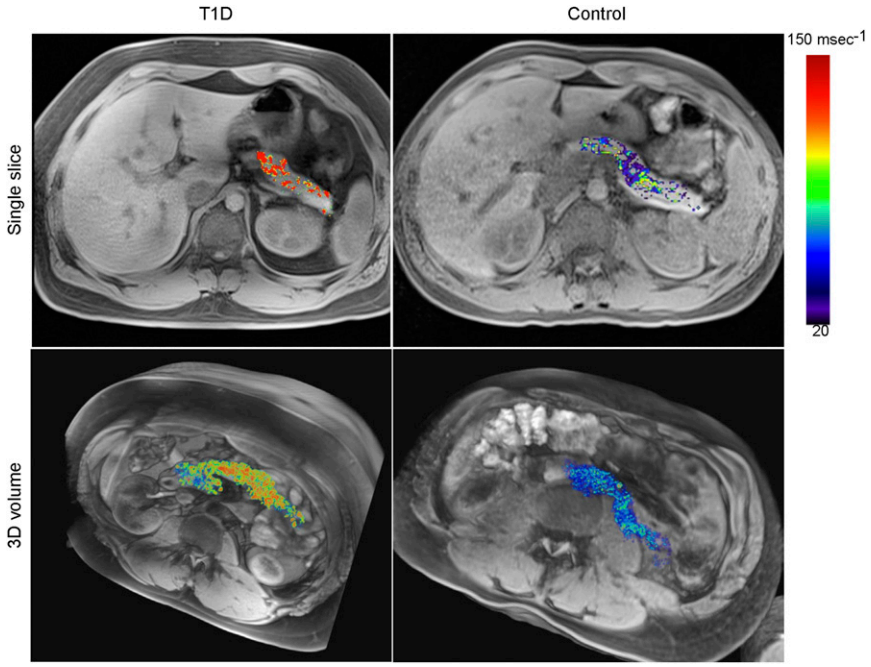

Fig. 2. Increased pancreatic nanoparticle accumulation in patients with T1D. Single-slice (*Upper Row*) and 3D volume sets (*Lower Row*) of a representative patient with recently diagnosed T1D (*Left*) and a normal control subject (*Right*).

Global ΔR2* Metric. For pancreas-wide quantification of nanoparticle uptake, we calculated a global ΔR2* signal for each study subject by averaging R2* over the entire volume of the pancreas and subtracting the preinfusion value from the 48-h postinfusion value, without a voxel transform (Fig. 5 and Table 1). There was good separation between patients with recent-onset T1D and normal controls. The subtractions resulted in negative numbers in two normal controls. In general, these global values reflected the images shown in Fig. 4 and, although they ignore details of the spatial distribution of inflammation, provide statistical

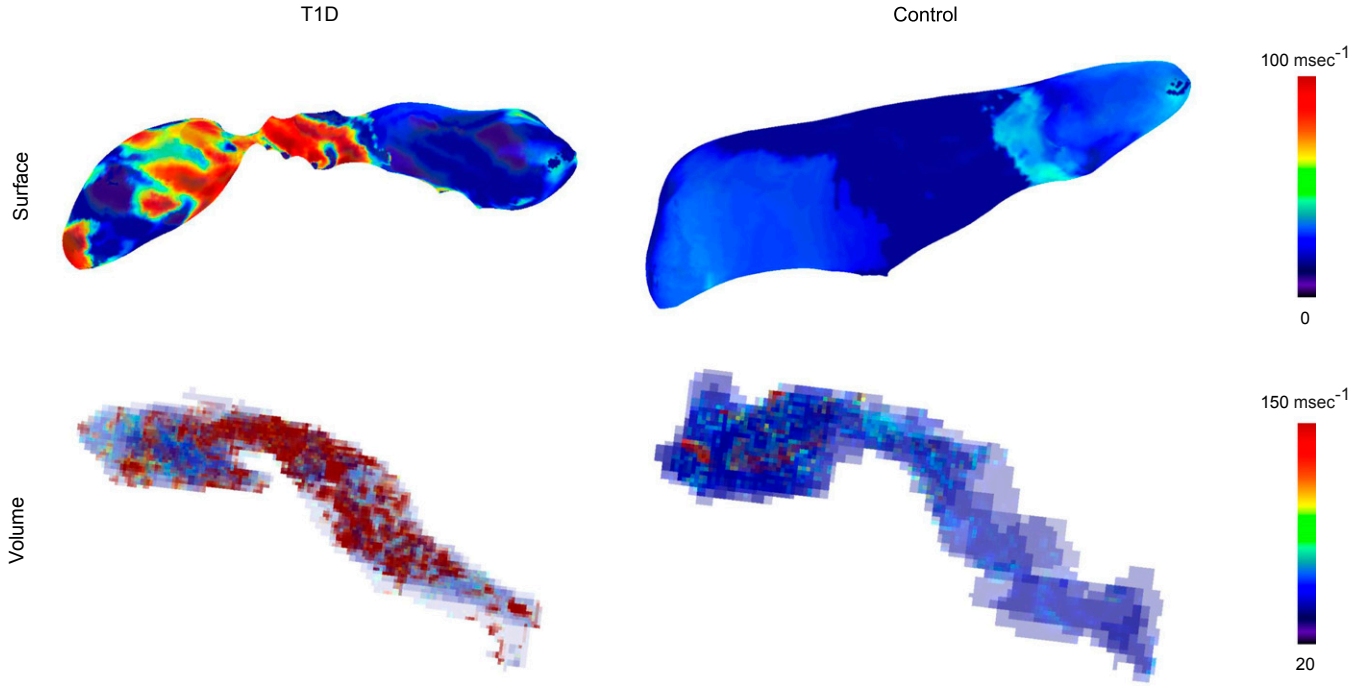

Fig. 3. Visualization of intrapancreatic heterogeneity of nanoparticle accumulation. Two different visualization models were used to display pancreatic distributions of ferumoxytol uptake. (*Upper*) Representative examples of surface mapping. With this method, all intrapancreatic voxels are transposed to the surface, more heavily weighting those closer to the surface and thus producing a map representing the near-surface inflammation values. For better visualization, we computationally inflated pancreatic surfaces. (*Lower*) See-through models of pancreata without surface weighting, which show intraparenchymal heterogeneity of nanoparticle accumulation.

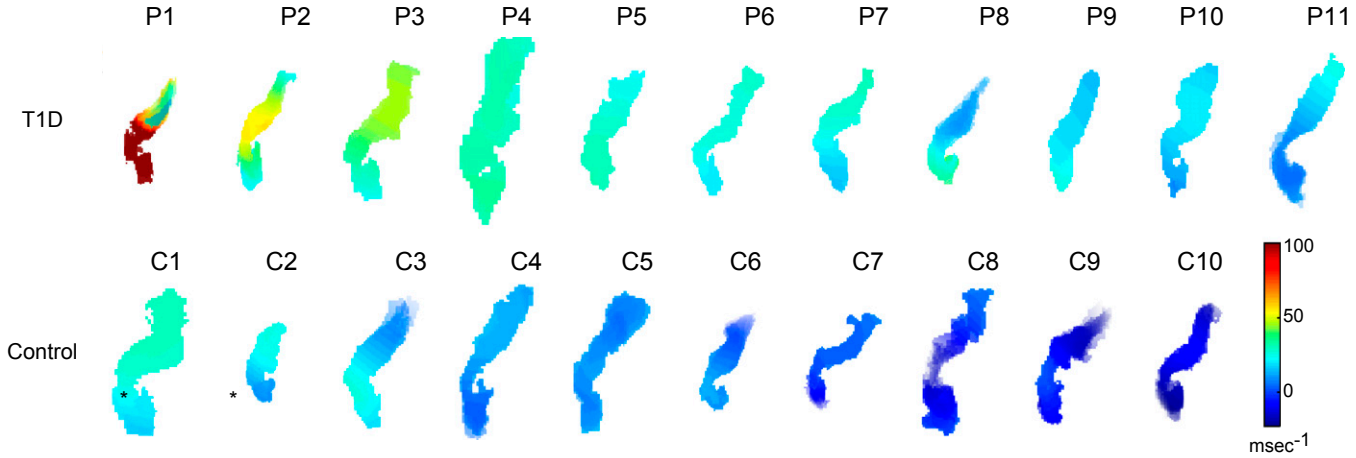

Fig. 4. Pancreatic surface maps of all patients studied. ΔR2* maps are shown for the T1D (*Upper*) and control (*Lower*) groups. The values were spatially low-pass filtered for better visualization and easier comparison. The images were sorted with respect to their mean ΔR2* maps, descending from left to right; negative values are not shown. Pancreata from the two starred control subjects correspond to the two uppermost controls in Fig. 5, which overlap with values for the T1D group.

justification for the application of this technique to imaging pancreatic inflammation in T1D.

Discussion

The goal of this study was to develop an accurate and exportable method for noninvasive visualization of pancreatic inflammation in patients with T1D. We achieved this goal by means of 3T MRI of the new-generation, clinically approved nanoparticle ferumoxytol. Success depended on extensive optimization of protocols for image acquisition and on innovative approaches to image analysis. This method permitted most patients with recent-onset T1D to be distinguished from most healthy controls and, for the first time (to our knowledge), revealed intrapancreatic heterogeneity in inflammatory manifestations in live individuals.

Ferumoxytol, a drug clinically approved for treatment of iron deficiency anemia in adult patients with chronic kidney disease (26, 27), can be used repeatedly as long as iron levels are monitored. This nanoparticle consists of an iron oxide core with superparamagnetic properties detectable by MRI. The elemental iron of this core ultimately is incorporated into hemoglobin, hence its therapeutic utility. The particle is stabilized by a polymeric dextran coating, which is responsible for efficient accumulation in tissue macrophages throughout various organs. Where there is inflammation, resident and/or recruited macrophages efficiently engulf this material, leading to tissue changes quantifiable by MRI, even if the microscopic distribution is below the resolution threshold. In other words, islet accumulation of probe changes the magnetic properties of voxels in sufficient amounts to be detectable. This

Table 1. Clinical characteristics of individual study subjects

							HLA type						
Subject ID	Age, y	BMI	IA2A, IU/mL	GADA, IU/mL	ZnT8A, IU/mL	A1c, %	*DRB1A*	*DQA1A*	*DQB1A*	*DRB1B*	*DQA1B*	*DQB1B*	ΔR2*, ms^{-1}
P1	38	20.8	Neg	51	Neg	5.8	0301	0501	0201	0401	0301	0302	34.6
P2	21	20.4	367	240	Neg	9.3	0301	0501	0201	0701	0201	0202	57.3
P3	20	23.9	Neg	319	Neg	5.6	0301	0501	0201	0402	0301	0302	40.8
P4	20	30.2	320	366	0.779	5.6	0301	0501	0201	0301	0501	0201	25.2
P5	29	23.0	375	875	0.563	6.2	0402	0301	0302	1104	0505	0301	37.7
P6	28	21.0	358	209	0.186	7.3	0101	0101	0501	0401	0301	0302	29.6
P7	25	23.9	329	910	0.143	7.1	0701	0201	0202	1201	0505	0301	32.2
P8	19	24.5	57	318	0.034	6.7	0301	0501	0201	0401	0303	0501	25.9
P9	21	33.2	329	910	0.143	6.0	0401	0301	0301	0901	0301	0303	27.3
P10	31	23.1	Neg	757	0.051	7.1	0101	0101	0501	0101	0101	0501	29.6
P11	26	21.9	284	945	0.116	6.8	0701	0201	0202	1301	0102	0604	24.0
C1	26	27.0	Neg	Neg	Neg	5.0	0701	0201	0202	1104	0505	0301	29.2
C2	28	29.9	Neg	Neg	Neg	5.3	0301	0501	0201	1302	0102	0604	11.9
C3	32	22.6	Neg	Neg	Neg	5.6	0101	0101	5014	1501	0102	0602	19.7
C4	29	25.7	Neg	Neg	Neg	5.4	0402	0301	0302	1501	0102	0602	14.6
C5	28	20.2	Neg	Neg	Neg	4.9	ND	ND	ND	ND	ND	ND	29.8
C6	30	30.2	Neg	Neg	Neg	5.7	0702	0201	0202	0701	0201	0202	12.7
C7	28	20.9	Neg	Neg	Neg	5.4	0401	0301	0302	1201	0505	0301	17.5
C8	26	23.2	Neg	Neg	Neg	5.4	0301	0501	0201	1302	0102	0604	−6.1
C9	24	22.4	Neg	Neg	Neg	5.3	0102	0101	0501	0404	0301	0302	13.4
C10	21	22.0	Neg	Neg	Neg	4.5	0101	0101	0501	1501	0102	0602	−11.3

AutoAb values considered positive: IA2A >7; GADA >25; ZnT8A >0.030. A1c, hemoglobin A1c; BMI, body-mass index; ND, not determined; Neg, negative.

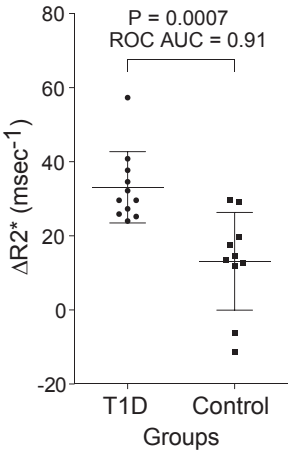

Fig. 5. Comparison of the two cohorts examined by MRI. Plots of global pancreatic ΔR2* values are shown for 11 patients with autoAb-confirmed T1D and 10 normal controls. The volume-averaged subtractions resulted in negative numbers in two normal controls. The *P* value was determined by the Mann–Whitney *u* test.

strategy is analogous to microvascular functional MRI approaches that use similar materials.

In feasibility studies leading to the current trial, we performed a dose-escalation study and confirmed that an ideal imaging dose is ∼4 mg Fe/kg body weight or ∼280 mg per average patient. This dose is well below the therapeutic dose (510 mg Fe followed by a second 510-mg Fe dose 3–8 d later). Lower doses resulted in less pronounced imaging effects; higher doses did not contribute to the differentiation between patients with T1D and controls. Coupled with significant technical advances in MRI technology—including higher field strengths, advanced phased array coils, and sequence optimization for enhanced resolution—it now is possible to obtain high-resolution maps (voxel size: 1.98 × 1.98 × 4 mm resliced to isotropic 1.1 mm^3) of the entire pancreas within 30–45 min.

How does imaging compare with other biomarkers of T1D? We did not find a correlation between MRI signals and either autoAb titers or the number of autoAbs detected. This finding is not entirely surprising because autoAb titers are only a remote measure of what is occurring in the pancreas. Indeed, they have neither predicted nor been correlated with response to immunomodulatory therapies in most clinical trials (28, 29). Interestingly, in one individual who was excluded a priori from the study because T1D could not be confirmed by measuring autoAbs, we were able to demonstrate inflammation of the pancreas using our imaging methodology (ΔR2* = 35.3 ms^{-1}). Therefore, identification of autoAb-negative individuals who have T1D is one potential use for this method.

Recently, a working histologic definition of insulitis was proposed based on the level of background T-cell infiltration seen in the parenchyma of nondiabetic donor pancreata (6). However, this background infiltration is highly variable and is dependent on conditions surrounding hospitalization and organ recovery (30). The MRI approach detailed here appears to be highly sensitive and does not have this limitation. In addition, there has been active discussion (and fewer data) on the extent to which humans typically show insulitis according to this T-cell–centric definition. As our imaging method quantifies nanoparticle accumulation within macrophages, established elements of both human and rodent pancreatic infiltrates, it side-steps this issue.

Nonetheless, there are some limitations to this study. For example, all study participants were at least 18 y old. Because there is age-dependent variation in disease progression, with an older age at diagnosis being associated with slower evolution, younger individuals may have even more pronounced pancreatic changes than observed here (7). Fortunately, MRI of nanoparticles does not involve radiation, a major concern with pediatric populations.

The MRI method detailed here is ready for application in multitudinous clinical studies. The most immediate use is likely to be monitoring an individual's response to immunomodulatory therapies. Imaging the same individual before and at different times after drug treatment should enhance further the quality and thereby utility of the data. This application has been modeled successfully in NOD mice (16). Also begging for exploration is the utility of this approach in predicting eventual onset of diabetes in high-risk individuals or as a stratification method in clinical trials, applications again validated in the NOD model (11). Last, the approach should be applicable to other autoimmune or inflammatory diseases that target difficult-to-access organs.

Materials and Methods

Study Participants and Clinical Assays. All participants were 18 y of age or older. Informed consent was obtained after the nature and possible consequences of the studies were explained. Participation entailed enrollment in two protocols, one at Joslin Diabetes Center for measurement of immune and metabolic parameters and one at Massachusetts General Hospital for imaging (ClinicalTrials.gov NCT01521520). The Joslin Diabetes Center Committee on Human Studies and the Massachusetts General Hospital Institutional Review Board approved the protocols. FDA Investigational New Drug approval was obtained for the use of ferumoxytol for MRI.

Controls had no known personal or family history of T1D, no relevant autoAbs (insulin, GAD, IA2, or ZnT8), normal hemoglobin A1c, and normal blood sugar after a mixed-meal tolerance test. Individuals with recent-onset T1D were within 6.5 mo of clinical diagnosis and had at least one detectable autoAb from the group GAD, IA2, and ZnT8. Investigators performing image acquisition and analysis were masked as to the diabetes status of study participants. No immediate contrast-related reactions were identified during the study.

AutoAbs were titered by the Barbara Davis Center for Diabetes. GAD65 (GADA), IA-2 (IA2A), and ZnT8 (ZnT8A) autoAbs were quantified by radiobinding assays. The GADA and IA2A assays are National Institutes of Health/National Institute of Diabetes and Digestive and Kidney Diseases harmonized assays with results expressed as digestive and kidney disease units/mL. HLA typing for DRB1 and DQA and B was done by the Barbara Davis Center for Diabetes.

Nanoparticles. We used the MNP ferumoxytol (Feraheme; AMAG Pharmaceuticals) (Fig. S3). Ferumoxytol currently is approved in North America and Europe as an iron-replacement therapy in adults with chronic kidney disease and can be given repeatedly. It has an average colloidal particle size of 30 nm by light scattering (range 17–31 nm) and a molecular mass of 750 kDa. It is comprised of a nonstoichiometric magnetite core in a semisynthetic carbohydrate coating of polyglucose sorbitol carboxymethyl ether designed to minimize immunological sensitivity. The blood half-life [∼14.5 h at a dose of 4 mg/kg (18)] is dose-dependent, with a shorter intravascular half-life at lower concentrations. Ferumoxytol is packaged as a sterile, neutral pH liquid containing 30 mg of elemental iron/mL. Prior studies in mouse models of diabetes had shown that the polymer-coated nanoparticle accumulates primarily in macrophages of inflamed pancreata and can distinguish diabetic from nondiabetic NOD mice. Ferumoxytol also has been used for prior MRI studies on lymph nodes (31) and for MR angiography (32).

MRI. MRI of the abdomen was performed before and 48 h after i.v. administration of ferumoxytol. T1-, T2-, and T2*-weighted MRI of the upper abdomen was done on a commercially available and clinically approved 3T MRI system (Trio Tim; Siemens) with a 45 mT/m maximum gradient capability and a slew rate of 200 T·m^{-1}·s^{-1}. We used a combination of an anterior body array matrix coil and a posterior spine coil. After acquisition of scout images, high-resolution axial T1-weighted, T2-weighted, and T2*-weighted sequences were obtained before and 2 d after a 5-min i.v. administration of ferumoxytol. High-resolution axial T2-weighted images were obtained using a high-resolution turbo spin-echo sequence using radially oriented blades with oversampling of the central k-space to reduce motion artifact [repetition time (TR)/effective echo time (TE$_{eff}$), 2,710 ms/112 ms; flip angle, 150°; six evenly spaced rotating blades of echo train length 27; 75% k-space

coverage; section thickness, 4 mm with 20% intersection gap; field of view (FOV), 450 × 450 mm; matrix, 256 × 256; voxel size, 1.8 × 1.8 × 4 mm; generalized autocalibrating partially parallel acquisitions (GRAPPA) with parallel imaging factor of 2; receiver bandwidth, 592 Hz per voxel; one signal average; total acquisition time, 1 min 16 s over four concatenations]. In addition, an axial T2-weighted 3D sequence called "sampling perfection with the application of optimized contrasts using different flip angle evolution" (SPACE), with isotropic voxels of ~1 mm [TR/TE, 3,000/579 ms; FOV, 275 × 275 mm; number of excitations, 2; sections per slab, 208; parallel acquisition techniques, 2; parallel acquisition techniques mode, GRAPPA; echo spacing, 3.34 ms; turbo factor, 173; section turbo factor, 2; flip angle mode, T2 variant (variable flip angle mode); acquisition time, 6.24 min] was performed also. Axial T1-weighted images were obtained using a T1-weighted volumetric interpolated gradient-echo (volumetric interpolated breath-hold examination; VIBE) sequence (TR/TE, 4.3/1.7 ms; flip angle, 10°; slice thickness, 3.5 mm; gap, 0; mean number of slices, 72 ± 15.2; range, 35–80 slices; FOV, 360 mm; matrix size, 144 × 320; phase × frequency; acquisition time, 19 s). Quantitative axial T2* sequences were performed as breath-hold, monopolar, multiecho, gradient echo sequences with six in-phase, equally spaced echoes (TE, 2.5–14.8 ms; TR, = 169 ms; thickness = 4 mm) in all patients. Imaging time ranged from 35–45 min per subject.

Data Analysis. Pancreas maps were generated by first up-sampling the R2* series to isotropic voxels, then registering the 48-h postinfusion image of each subject to the preinfusion image, computing the ΔR2* image by transforming the 48-h postinfusion R2* image (using the computed deformation field), and subtracting the baseline R2* image from it. To obtain the deformation field, the registration was done by first linearly aligning (33) manually created masks of the pancreas, the results from which were used to initialize the deformable alignment, which was performed in turn using the diffeomorphic demons registration of the National Library of Medicine Insight Segmentation and Registration Toolkit (34). To improve the mask registration, a signed distance transform was used (35). To create 3D surface maps, the R2* images were registered to the T1 images, the pancreatic T1 surfaces were extracted, and the near-surface ΔR2* values were projected onto the T1 surfaces. The pancreatic surfaces then were inflated, providing a more regular representation of the surface that still retained much of the shape and metric properties of the original pancreatic surface. Thus, better visualization of inflammatory changes was provided by the removal of any surface irregularities. Pancreatic surface extraction and inflation were performed using FreeSurfer software (23, 36, 37). Relevant equations are presented in Fig. S4.

Statistics. Results for continuous variables are expressed as mean ± SD. The Mann–Whitney *u* test was used for between-group comparisons of patients with T1D and healthy controls. Correlation was evaluated using Spearman's rank correlation coefficient.

ACKNOWLEDGMENTS. This work was supported by NIH Grant P01-AI-054904; NIH Grant R01-NS083534 (to Bruce Fischl); NIH Grants U01-HL080731, P50-CA86355, U54-CA119349, and U24-CA092782 (for technology development); NIH Grant P30-DK036836; NIH Grant KL2-TR001100; and philanthropic donors to the Joslin Clinical Research Center.

1. Herold KC, Vignali DA, Cooke A, Bluestone JA (2013) Type 1 diabetes: Translating mechanistic observations into effective clinical outcomes. *Nat Rev Immunol* 13(4): 243–256.
2. Achenbach P, et al. (2013) Characteristics of rapid vs slow progression to type 1 diabetes in multiple islet autoantibody-positive children. *Diabetologia* 56(7):1615–1622.
3. Verge CF, et al. (1996) Prediction of type I diabetes in first-degree relatives using a combination of insulin, GAD, and ICA512bdc/IA-2 autoantibodies. *Diabetes* 45(7): 926–933.
4. Sosenko JM, et al.; Type 1 Diabetes TrialNet Study Group; Diabetes Prevention Trial-Type 1 Study Group (2013) The prediction of type 1 diabetes by multiple autoantibody levels and their incorporation into an autoantibody risk score in relatives of type 1 diabetic patients. *Diabetes Care* 36(9):2615–2620.
5. Ziegler AG, et al. (2013) Seroconversion to multiple islet autoantibodies and risk of progression to diabetes in children. *JAMA* 309(23):2473–2479.
6. Campbell-Thompson ML, et al. (2013) The diagnosis of insulitis in human type 1 diabetes. *Diabetologia* 56(11):2541–2543.
7. In't Veld P (2011) Insulitis in human type 1 diabetes: The quest for an elusive lesion. *Islets* 3(4):131–138.
8. Pugliese A, et al. (2014) New insight on human type 1 diabetes biology: nPOD and nPOD-transplantation. *Curr Diab Rep* 14(10):530.
9. Papaccio G (1993) Insulitis and islet microvasculature in type 1 diabetes. *Histol Histopathol* 8(4):751–759.
10. De Paepe ME, Corriveau M, Tannous WN, Seemayer TA, Colle E (1992) Increased vascular permeability in pancreas of diabetic rats: Detection with high resolution protein A-gold cytochemistry. *Diabetologia* 35(12):1118–1124.
11. Denis MC, Mahmood U, Benoist C, Mathis D, Weissleder R (2004) Imaging inflammation of the pancreatic islets in type 1 diabetes. *Proc Natl Acad Sci USA* 101(34): 12634–12639.
12. Signore A, et al. (1996) In vivo measurement of immunoglobulin accumulation in the pancreas of recent onset type 1 diabetic patients. *Clin Exp Rheumatol* 14(Suppl 15): S41–S45.
13. Jansen A, et al. (1994) Immunohistochemical characterization of monocytes-macrophages and dendritic cells involved in the initiation of the insulitis and beta-cell destruction in NOD mice. *Diabetes* 43(5):667–675.
14. Hanenberg H, Kolb-Bachofen V, Kantwerk-Funke G, Kolb H (1989) Macrophage infiltration precedes and is a prerequisite for lymphocytic insulitis in pancreatic islets of pre-diabetic BB rats. *Diabetologia* 32(2):126–134.
15. Fu W, Wojtkiewicz G, Weissleder R, Benoist C, Mathis D (2012) Early window of diabetes determinism in NOD mice, dependent on the complement receptor CRIg, identified by noninvasive imaging. *Nat Immunol* 13(4):361–368.
16. Turvey SE, et al. (2005) Noninvasive imaging of pancreatic inflammation and its reversal in type 1 diabetes. *J Clin Invest* 115(9):2454–2461.
17. Gaglia JL, et al. (2011) Noninvasive imaging of pancreatic islet inflammation in type 1A diabetes patients. *J Clin Invest* 121(1):442–445.
18. Landry R, Jacobs PM, Davis R, Shenouda M, Bolton WK (2005) Pharmacokinetic study of ferumoxytol: A new iron replacement therapy in normal subjects and hemodialysis patients. *Am J Nephrol* 25(4):400–410.
19. Wood JC, et al. (2005) MRI R2 and R2* mapping accurately estimates hepatic iron concentration in transfusion-dependent thalassemia and sickle cell disease patients. *Blood* 106(4):1460–1465.
20. Altobelli E, et al. (1998) Size of pancreas in children and adolescents with type I (insulin-dependent) diabetes. *J Clin Ultrasound* 26(8):391–395.
21. Goda K, et al. (2001) Pancreatic volume in type 1 and type 2 diabetes mellitus. *Acta Diabetol* 38(3):145–149.
22. Williams AJ, Chau W, Callaway MP, Dayan CM (2007) Magnetic resonance imaging: A reliable method for measuring pancreatic volume in Type 1 diabetes. *Diabet Med* 24(1):35–40.
23. Fischl B, Sereno MI, Dale AM (1999) Cortical surface-based analysis. II: Inflation, flattening, and a surface-based coordinate system. *Neuroimage* 9(2):195–207.
24. Alanentalo T, et al. (2010) Quantification and three-dimensional imaging of the insulitis-induced destruction of beta-cells in murine type 1 diabetes. *Diabetes* 59(7): 1756–1764.
25. In't Veld P (2014) Insulitis in human type 1 diabetes: A comparison between patients and animal models. *Semin Immunopathol* 36(5):569–579.
26. McCormack PL (2012) Ferumoxytol: In iron deficiency anaemia in adults with chronic kidney disease. *Drugs* 72(15):2013–2022.
27. Lu M, Cohen MH, Rieves D, Pazdur R (2010) FDA report: Ferumoxytol for intravenous iron therapy in adult patients with chronic kidney disease. *Am J Hematol* 85(5): 315–319.
28. Herold KC, et al.; AbATE Study Team (2013) Teplizumab (anti-CD3 mAb) treatment preserves C-peptide responses in patients with new-onset type 1 diabetes in a randomized controlled trial: Metabolic and immunologic features at baseline identify a subgroup of responders. *Diabetes* 62(11):3766–3774.
29. Petersen JS, et al.; The Canadian-European Randomized Control Trial Group (1994) Glutamic acid decarboxylase (GAD65) autoantibodies in prediction of beta-cell function and remission in recent-onset IDDM after cyclosporin treatment. *Diabetes* 43(11): 1291–1296.
30. In't Veld P, et al. (2010) Beta-cell replication is increased in donor organs from young patients after prolonged life support. *Diabetes* 59(7):1702–1708.
31. Harisinghani M, Ross RW, Guimaraes AR, Weissleder R (2007) Utility of a new bolus-injectable nanoparticle for clinical cancer staging. *Neoplasia* 9(12):1160–1165.
32. Weissleder R, Nahrendorf M, Pittet MJ (2014) Imaging macrophages with nanoparticles. *Nat Mater* 13(2):125–138.
33. Reuter M, Rosas HD, Fischl B (2010) Highly accurate inverse consistent registration: a Robust approach. *Neuroimage* 53(4):1181–1196.
34. Vercauteren T, Pennec X, Perchant A, Ayache A (2007) Diffeomorphic demons using ITK's finite difference solver hierarchy. *The Insight Journal - 2007 MICCAI Open Science Workshop.* Available at hdl.handle.net/1926/510. Accessed January 20, 2015.
35. Kozinskaa D, Tretiakb OJ, Nissanovb J, Ozturkb C (1997) Multidimensional alignment using the euclidean distance transform. *Graph Models Image Proc* 59(6):373–387.
36. Dale AM, Fischl B, Sereno MI (1999) Cortical surface-based analysis. I. Segmentation and surface reconstruction. *Neuroimage* 9(2):179–194.
37. Fischl B (2012) FreeSurfer. *Neuroimage* 62(2):774–781.